Acta Pharmaceutica Sinica B 2022;12(4):2014–2028

Chinese Pharmaceutical Association
Institute of Materia Medica, Chinese Academy of Medical Sciences

Acta Pharmaceutica Sinica B

www.elsevier.com/locate/apsb
www.sciencedirect.com

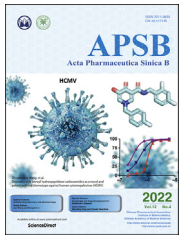

ORIGINAL ARTICLE

Osteopontin targeted theranostic nanoprobes for laser-induced synergistic regression of vulnerable atherosclerotic plaques

Mengqi Xu[a,†], Cong Mao[b,†], Haoting Chen[b], Lu Liu[c], Yabin Wang[a], Abid Hussain[c], Sulei Li[a], Xu Zhang[d], Ruslan G. Tuguntaev[b,*], Xing-Jie Liang[c], Weisheng Guo[b,*], Feng Cao[a,*]

[a]*Department of Cardiology, National Clinical Research Center for Geriatric Diseases & Second Medical Center of Chinese PLA General Hospital, Beijing 100853, China*
[b]*Department of Minimally Invasive Interventional Radiology, Key Laboratory of Molecular Target & Clinical Pharmacology, School of Pharmaceutical Sciences & the Second Affiliated Hospital, Guangzhou Medical University, Guangzhou 510260, China*
[c]*Laboratory of Controllable Nanopharmaceuticals, Chinese Academy of Sciences (CAS) Center for Excellence in Nanoscience and CAS Key Laboratory for Biomedical Effects of Nanomaterials and Nanosafety, National Center for Nanoscience and Technology, Beijing 100190, China*
[d]*Department of Urology, Chinese PLA General Hospital, Beijing 100853, China*

Received 27 September 2021; received in revised form 30 November 2021; accepted 5 December 2021

KEY WORDS

Vulnerable atherosclerotic plaques;
Theranostic nanoprobe;
Human serum albumin;
Osteopontin;
Photodynamic therapy;
Hypoxia;
Reactive oxygen species;
Tirapazamine

Abstract Vulnerable atherosclerotic plaque (VASPs) is the major pathological cause of acute cardiovascular event. Early detection and precise intervention of VASP hold great clinical significance, yet remain a major challenge. Photodynamic therapy (PDT) realizes potent ablation efficacy under precise manipulation of laser irradiation. In this study, we constructed theranostic nanoprobes (NPs), which could precisely regress VASPs through a cascade of synergistic events triggered by local irradiation of lasers under the guidance of fluorescence/MR imaging. The NPs were formulated from human serum albumin (HSA) conjugated with a high affinity-peptide targeting osteopontin (OPN) and encapsulated with photosensitizer IR780 and hypoxia-activatable tirapazamine (TPZ). After intravenous injection into atherosclerotic mice, the OPN-targeted NPs demonstrated high specific accumulation in VASPs due to the overexpression of OPN in activated foamy macrophages in the carotid artery. Under the visible guidance of fluorescence and MR dual-model imaging, the precise near-infrared (NIR) laser irradiation generated

*Corresponding authors.
E-mail addresses: rus_taev89@mail.ru (Ruslan G. Tuguntaev), tjuguoweisheng@126.com (Weisheng Guo), fengcao8828@163.com (Feng Cao).
[†]These authors made equal contributions to this work.
Peer review under responsibility of Chinese Pharmaceutical Association and Institute of Materia Medica, Chinese Academy of Medical Sciences.

https://doi.org/10.1016/j.apsb.2021.12.020

massive reactive oxygen species (ROS), which resulted in efficient plaque ablation and amplified hypoxia within VASPs. In response to the elevated hypoxia, the initially inactive TPZ was successively boosted to present potent biological suppression of foamy macrophages. After therapeutic administration of the NPs for 2 weeks, the plaque area and the degree of carotid artery stenosis were markedly reduced. Furthermore, the formulated NPs displayed excellent biocompatibility. In conclusion, the developed HSA-based NPs demonstrated appreciable specific identification ability of VASPs and realized precise synergistic regression of atherosclerosis.

1. Introduction

Atherosclerosis (AS) is the leading cause of cardiovascular disease (CVD) including myocardial infarction (MI), stroke and heart failure[1,2]. Atherosclerosis is primarily located in the intima of many middle and large sized arteries, where the oxidized low-density lipoprotein (ox-LDL) are in abundance[3]. Macrophages hold a dominant role as key orchestrators associated with the progression of AS by ingesting the deposited ox-LDL resulting in the formation of foamy macrophages[4]. The increased amount of foamy cells secrete inflammatory cytokines leading to atherosclerotic plaque vulnerability that may lead to higher risk of hemorrhage/rapture[5]. Increased evidence has documented that the abundance of foamy macrophages within plaques is correlated with the decades-long lasting asymptomatic pathogenesis of AS in the clinic[6,7]. Therefore, accurately identifying the vulnerable atherosclerotic plaques (VASPs) in the early stage of AS, assessing the risk of acute coronary syndrome, and taking effective interventions are essential to prevent the occurrence of life-threatening events.

Early identification of AS depends on biomedical imaging technologies, such as ultrasonography and computed tomography angiography are widely used for non-invasive investigation of plaques in various vascular territories[8,9]. Moreover, some mini-invasive procedures, such as invasive angiography, intravascular ultrasonography and/or optical coherence tomography are also employed to evaluate the degree of vascular stenosis and plaque characteristics in clinical practice[10,11]. However, these approaches have limitations in assessing molecular characteristics of plaques and dynamically monitoring the AS progression[12,13]. Moreover, they are incapable of accurately distinguishing the inflammation and cellular activity in vulnerable plaques from a stable lesion[14,15]. Current therapy for arterial severe stenosis caused by vulnerable plaque mostly depends highly on invasive therapy and surgery[3,11,16–18]. Therefore, it is of great clinical significance to realize accurate identification as well as targeted therapy of vulnerable plaque simultaneously. Recent advances in the field of nanotechnology research presenting promising combination comprising diagnostic and therapeutic delivery modalities, leading towards more detailed diagnostic readouts and the site-specific therapy[19–22]. Furthermore, target-specific molecular markers of VASPs can achieve multimodal plaque imaging and improve the therapeutic effect of anti-atherosclerotic drugs[23]. Osteopontin (OPN) is highly overexpressed at the sites of atherosclerosis plaques particularly those associated with foamy macrophage cells[24,25]. The OPN has been studied extensively as a biomarker secreted in a large amount by foam cells, thus possesses great significance to evaluate the progression of atherosclerosis[26,27]. Therefore, multi-purpose nanomaterials with highly selective targeting moieties provide great potentials to overcome the issues associated with AS therapy and noninvasive recognition of VASPs.

Moreover, activatable theranostics are emerging as an attractive approach to early diagnosis, precise intervention treatment and even prognostic monitoring of diseases with aid of biomedical imaging techniques[28]. Photodynamic therapy (PDT) is realized *via* the generation of reactive oxygen species (ROS) by photosensitizers under laser irradiation[29]. The applications of PDT have been extended to a variety of diseases, including skin disorders, cancers, and atherosclerosis[29–31], due to the advantages of spatiotemporal selectivity, reduced side effects, and minimal invasiveness[32]. Nevertheless, the application of PDT results in an aggregated hypoxia microenvironment because of the consumption of oxygen in specific tissue[33–35]. The resulting hypoxia has considerable limitations to the therapeutic efficacy of PDT.

Considering the challenges and principles mentioned above, we have successfully constructed a human serum albumin (HSA)-based theranostic nanoprobes (TPZ/IR780@HSA−OPN NPs) which could precisely regress the VASPs through a cascade of synergistic events triggered by careful lasers irradiation under the guidance of fluorescence/MR imaging. The TPZ/IR780@HSA−OPN NPs were formulated from HSA decorated with a high affinity-peptide targeting OPN and encapsulated with photosensitizer IR780 and hypoxia-activatable tirapazamine (TPZ). As illustrated in Scheme 1, after intravenous injection into atherosclerotic mice, the HSA-based NPs demonstrated high specific accumulation ability in the region of VASPs due to the overexpression of OPN in activated foamy macrophages in the carotid artery. Under the visible guidance of fluorescence and MR dual-model imaging, precise near-infrared (NIR) laser irradiation led to efficient plaque ablation as well as amplified hypoxia within VASPs. As a result, the payload of TPZ that has initial inactivity was elicited to display potent biological suppression of foamy macrophages under NIR laser irradiation. The animal experiments verified that the plaque area and the degree of carotid artery stenosis were markedly reduced after therapeutic administration of the TPZ/IR780@HSA−OPN NPs for 2 weeks. In conclusion, the developed HSA-based NPs demonstrated highly accurate identification ability of VASPs and realized precise synergistic regression of atherosclerosis.

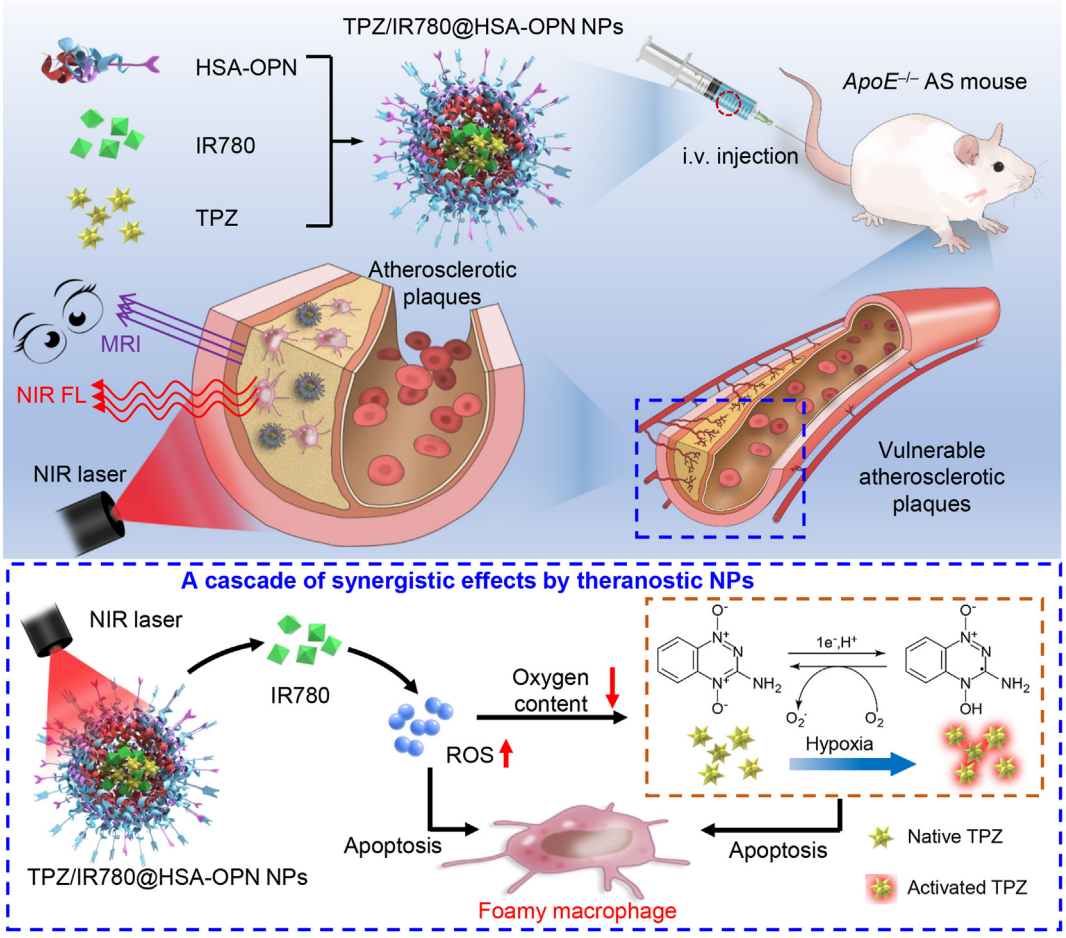

Scheme 1 Schematically illustrate construction of theranostic TPZ/IR780@HSA−OPN NPs, which could precisely regress the VASPs through a cascade of synergistic events triggered by careful lasers irradiation under the guidance of NIR fluorescence/MR imaging.

2. Materials and methods

2.1. *Materials*

Tirapazamine (TPZ), IR780 and human serum albumin (HSA) were purchased from Sigma−Aldrich Co., Ltd. (St. Louis, MO, USA). antiOPN peptide was obtained from ChinaPeptides Co., Ltd. (Shanghai, China). Glutaraldehyde was purchased from Aladdin Co., Ltd. (Shanghai, China). RPMI 1640 medium were purchased from HyClone (Logan, UT, USA) and fetal bovine serum (FBS) was obtained from Gibco (Grand Island, NE, USA). FITC-conjugated secondary antibody and ox-LDL were purchased from Bioss (Beijing, China). OPN primary antibody, β-actin antibody and HRP-conjugated secondary antibody was purchased from Abcam (Cambridge, UK). Paraformaldehyde (PA), Triton X-100, Bovine serum albumin (BSA), 4′,6-diamidino-2-phenylindole (DAPI), RIPA, PMSF, Tris buffered saline-Tween-20 (TBST) were obtained from Solarbio Co., Ltd. (Beijing, China). BCA Protein Assay Kit was acquired from Thermo Scientific Pierce (Rockford, IL, USA). Polyvinylidene difluoride (PVDF) membranes were purchased from Millipore (Burlington, MA, USA). Cell Counting Kit-8 was acquired from Dojindo Laboratories (Kyushu Island, Japan). Hypoxia/Oxidative Stress Detection Kit was purchased from Enzo Life Sciences (Farmingdale, NY, USA). Annexin V-FITC/PI Apoptosis Detection Kit was obtained from BD Biosciences (San Jose, CA, USA).

2.2. *Synthesis and characterization of TPZ/IR780@HSA−OPN NPs*

To obtain TPZ/IR780 core complexes, TPZ (1 mg) and IR780 (0.2 mg) in 0.2 mL DMSO were added dropwise into 1 mL of phosphate-buffered saline (PBS) containing 10 mg of human serum albumin (HSA). Afterward, in order to increase the stability of the protein nanoparticles, 3 μL of glutaraldehyde aqueous solution (5%, *v*/*v*) was added to the mixture, followed by vigorously stirring at 25 °C for 1 h. The HSA−OPN compound was prepared by mixing HSA (10 mg), antiOPN peptide (1 mg), and Sulf-SMCC (0.66 mg) in 0.4 mL H_2O with further stirring at 25 °C for 2 h. Then, the solution containing HSA−OPN conjugate was purified from the excess of OPN and Sulf-SMCC by washing with PBS in the Amicon centrifugal filter (molecular weight cut-off = 30 kDa). Finally, the TPZ/IR780@HSA−OPN NPs were fabricated by mixing of previously prepared solutions. Briefly, water solution (0.1 mL) of HSA−OPN was added dropwise into TPZ/IR780 in PBS (1 mL), and the mixture solution was then stirred at 25 °C for 30 min. The obtained TPZ/IR780@HSA−OPN NPs were then washed with PBS in the Amicon centrifugal filter

(molecular weight cut-off = 100 kDa) in order to remove free HSA−OPN. The control sample of TPZ/IR780@HSA was formulated following the same procedures as described above, except that the HSA−OPN was replaced with free HSA protein.

The size distributions and polydispersity index (PDI) of TPZ/IR780@HSA−OPN NPs and TPZ/IR780@HSA NPs were evaluated using Malvern Zetasizer (Malvern Instruments, Worcestershire, UK). The morphology and size of formulated NPs were observed with transmission electron microscopy (TEM, JEM-200CX, JEOL, Tokyo, Japan). The contents of HSA, TPZ and IR780 in the NPs were determined using the UV-2600i Spectrophotometer (SHIMADZU, Tokyo, Japan).

2.3. Cell culture and immunofluorescence in vitro

Murine macrophage line RAW 264.7 (Institute of Basic Medicine, Chinese Academy of Medical Sciences, Beijing, China) was cultured with RPMI 1640 supplemented with 10% FBS and maintained in an incubator containing 5% CO_2 at 37 °C. RAW 264.7 cells were seeded onto an eight-well chambered glass-bottom dish (Nunc Lab-Tek, ThermoFisher Scientific, USA) with a density of 2.5×10^4 cells per well. Foamy macrophage model was stimulated by ox-LDL (80 μg/mL) for 24 h. Then, foamy macrophages and control group were both fixed with 4% PA, permeabilized with 0.3% Triton X-100, blocked with 5% BSA solution successively. Afterward, cells were incubated with OPN primary antibody (1/100 dilution) at 4 °C overnight, washed with PBS solution three times and incubated with FITC-conjugated secondary antibody (1/100 dilution) for 1 h at room temperature. Nuclei were stained with DAPI and the samples were visualized under the confocal laser scanning microscope (CLSM, Olympus FV1000, Japan).

2.4. Cellular fluorescence imaging in vitro

RAW 264.7 cells were seeded onto an eight-well chambered glass-bottom dish. Foamy macrophage model was stimulated by ox-LDL for 24 h. Then, foamy macrophages and control group were incubated with TPZ/IR780@HSA−OPN or TPZ/IR780@HSA at a concentration of 40 μg/mL (IR780) for another 24 h. Moreover, antiOPN peptide was pre-added 1 h earlier than the NPs as a blocking group. After rinsing off the NPs by PBS solution, the cell samples were fixed with 4% PA. Nuclei were stained with DAPI and the samples were visualized under the CLSM (Olympus). Similarly, RAW 264.7 cells and the ox-LDL stimulated foamy macrophages were incubated with TPZ/IR780@HSA NPs and TPZ/IR780@HSA−OPN NPs, respectively. Flow cytometry (BD FACS Aria, Franklin Lakes, NJ, USA) was employed to determine the cellular uptake efficiency.

2.5. Intracellular ROS/hypoxia detection

RAW 264.7 cells were seeded onto an eight-well chambered glass-bottom dish and activated into foamy macrophages. The cell samples were incubated with free IR780 or TPZ/IR780@HSA−OPN NPs at a concentration of 40 μg/mL (IR780) for 24 h. Then the IR780 and NPs solutions were rinsed off and the hypoxia/oxidative stress detection mixture were added to samples following the manufacturer's instruction. ROS inducer deferoxamine (DFO) and hypoxia inducer pyocyanin (Pyo) were used as positive controls. After incubation, cells were exposed to 808 nm laser at 1.0 W/cm^2 for 5 min. Finally, nuclei were stained with DAPI and lysosomes were stained by Deep Red. Samples were visualized under the CLSM (Olympus, the excitation/emission wavelengths of ROS detector, hypoxia detector, DAPI, Deep Red were set at 488 nm/514 ± 10 nm, 543 nm/595 ± 20 nm, 405 nm/455 ± 20 nm, and 633 nm/665 ± 20 nm, respectively).

2.6. The efficacy of photodynamic therapy in vitro

Macrophages were seeded in 96-well plates with a density of 1×10^4 cells per well and activated into foamy macrophages. The cells were divided into three groups and treated with TPZ/IR780@HSA−OPN NPs without laser exposure, IR780@HSA−OPN NPs with laser exposure, and TPZ/IR780@HSA−OPN NPs with laser exposure. Drugs were diluted into different concentrations (IR780 0, 20, 40, 60, 80, and 100 μg/mL) and were added into different groups for 24 h. After incubation, the cells were then exposed to an 808 nm laser irradiation for 3 min at 1.5 W/cm^2 and were further incubated for 2 h. Then cell viability was detected by CCK-8 essay. 100 μL of RPMI 1640 medium and 10 μL of CCK-8 solution were added to each well. After incubation for 2 h, the absorbance at 450 nm was measured by the microplate reader (TECAN Spark, Switzerland). To detect the apoptosis rate of foamy macrophages after photodynamic therapy, Annexin V-FITC/PI Apoptosis Detection Kit was used. Briefly, cells were harvest after drug incubation and laser irradiation. Then each sample was stained with Annexin V-FITC and propidium iodide (PI) following the manufacturer's protocol. The apoptosis rate was analyzed by Flow Cytometry (BD FACS Aria, Franklin Lakes, NJ, USA).

2.7. Animal mode of carotid vulnerable atherosclerotic plaque

Male 7-week-old ApoE$^{-/-}$ C57BL/6 mice (purchased from Vital River, Beijing, China) were initially fed with a high fat diet (HFD, containing 15% fat and 1.25% cholesterol) for 2 weeks and then a polymethylpentene perivascular cast (Promolding, Netherlands) was placed around their left common carotid artery to modify the vascular shear stress[36,37]. Subsequently, the ApoE$^{-/-}$ mice were kept on the HFD for another 16 weeks. The mice fed with the standard low-fat diet for the same period of time served as negative controls. All animal procedures were performed following a protocol approved by the Animal Care and Use Committee of the Chinese PLA General Hospital and in accordance with the Care and Use of Laboratory Animals formulated by the National Society for Medical Research.

2.8. Fluorescence imaging in vivo and ex vivo

Mice were divided into three groups (n = 10), including AS mice + TPZ/IR780@HSA-OPN group, the AS mice + TPZ/IR780@HSA group, and the healthy control mice + TPZ/IR780@HSA−OPN group. Nanoprobes were injected into mice from each group through tail vein at a dose of 1 mg/kg IR780. All the mice were general anesthetized by isoflurane and placed into fluorescence imaging system (IVIS Spectrum, Perkin−Elmer, USA). Imaging was captured after nanoprobes injection at different time points (0.5, 1, 2, 4 and 8 h) with parameters as follows: binning (4), F/stop (1.2), exposure time (5.0 s), emission filter (IR780). For *ex vivo* study, mice were euthanized at 1 h post-injection and the vessels were harvested and subjected to *ex vivo* imaging. Region of interests were circled around the plaque areas and the fluorescence intensities were analyzed by Living Image

Software (name, version). After fluorecsence imaging *ex vivo* accomplished, the carotid tissues containing plaques were frozen in Optimum Cutting Temperature (OCT) compound and transverse cryosections were acquired preparing for immunofluorescent staining of OPN and CD68. All the immunofluorescent samples were viewed under CLSM (Olympus) to verify the accumulation of nanoprobes in the vulnerable atherosclerotic plaques.

2.9. MR imaging in vivo

The nanoprobes were couplied with chlorine e6 (Ce6) and then chelated to manganese ions to achieve *in vivo* MR imaging, which was implemented on a 7.0 T MRI system (BioSpec 70/20 USR, Bruker, Germany). The grouping was the same as the fluorescence imaging study. 150 μL nanoprobes were injected into mice through tail vein and T1-weighted MR images were acquired before and after nanoprobes injection at different time points (1, 2, 4 and 8 h) with T1_RARE sequence parameters as follows: TE = 5.35 ms, TR = 300 ms, NEX = 5.0, FA = 90°; MTX = 256 × 256, FOV = 25 × 25 mm, slices = 20.

For the therapeutic study, AS mice were divided into four groups (n = 10), including the TPZ/IR780@HSA−OPN NPs group without laser irradiation, IR780@HSA−OPN NPs with laser irradiation, TPZ/IR780@HSA NPs with laser irradiation, and TPZ/IR780@HSA−OPN NPs with laser irradiation. All the AS mice initially received MR imaging 2 h after drug injection to obtain the MRI signal of carotid plaques. Then mice were intravenously injected with TPZ/IR780@HSA−OPN NPs (1 mg/kg IR780) or an equivalent dose of TPZ@HSA−OPN NPs and IR780@HSA−OPN NPs every other day for two weeks. One hour after drug injection, the left carotid area was irradiated under 808 nm laser source for 3 min at 0.75 W/cm^2. After PDT for two weeks, mice underwent MR imaging once again (same parameters as above). Time of flight (TOF) magnetic resonance angiography sequence was also performed to evaluate the improvement of carotid stenosis.

2.10. Tissue separation and pathological staining

To verify the vulnerable atherosclerotic plaque model and evaluate the PDT efficacy of NPs, the whole vessel from bilateral carotid artery to iliac artery was isolated from the mice after general anesthesia by isoflurane (RWD, Shenzhen, China). The arteries (n = 4) were fixed in 4% formaldehyde for 24 h, stained with oil red dye for 30 min and decolorized with 70% isopropanol until the vessel walls turned milky white. Segments from several carotid arteries (n = 6) were obtained and were fixed in a 4% PA for 24 h, embedded in paraffin, and sectioned at 5 μm thickness. Then hematoxylin-eosin (H&E) and Masson staining were performed to view the plaque morphology, followed by immunohistochemistry staining of CD68 and OPN to analyze the expression of OPN in the plaques. All images were observed under the light microscope (Olympus, Japan).

2.11. Western blot analysis

Cellular or tissue proteins were extracted by using RIPA and PMSF solution after macrophage samples were pre-treated with or without ox-LDL for 24 h. BCA Protein Assay Kit was used to determine the protein concentration. Proteins were separated by 10% SDS-PAGE and transferred onto polyvinylidene difluoride membranes. After blocking with 5% skim milk in TBST solution, the membranes were incubated with OPN primary antibodies (1/1000 dilution) and β-actin antibody (1:5000) at 4 °C overnight respectively. Subsequently, membranes were washed by TBST buffer and incubated with HRP-conjugated secondary antibody (1/5000 dilution) for 1 h at room temperature. The bands were visualized by enhanced chemiluminescence (ECL, Thermo Scientific Pierce, Rockford, IL, USA) and quantified by Image Lab software (Bio-Rad, Hercules, CA, USA).

2.12. Statistical data analysis

All data were presented as mean ± standard deviation (SD) and results were analyzed by GraphPad Prism 7 software (La Jolla, CA, USA). Comparison between two groups were made with two-tailed unpaired Student's t-tests, assuming a Gaussian distribution. The multi-group comparisons were made with a one-way ANOVA analysis, followed by Dunnet's post hoc test. Values of $P < 0.05$ were considered to be statistically significant.

3. Results and discussion

3.1. Evaluation of OPN expression in foamy macrophages and vulnerable atherosclerotic plaques

The progression of AS can be facilitated by the activation of macrophages within VASPs, which leads to the characteristic expression of synthetic marker OPN[38]. The overexpression of OPN in foamy macrophages can be explored for VASPs specific drug delivery. In this regard, we attempted to examine the expression levels of OPN in foamy macrophages by incubating RAW 264.7 cell lines with ox-LDL for 24 h. As shown in Fig. 1A and B, the immunofluorescence staining and Western blot analysis revealed a significant ($P < 0.01$) increase of OPN expression levels in foamy macrophages compared with the nontreated macrophages. Further, the expression level of OPN was also evaluated in a vulnerable plaque model in mice carotid artery. Western blot analysis showed that OPN expression was markedly increased in VASP compared with healthy vessel tissue ($P < 0.01$) (Fig. 1B). Various histological staining methods were employed to confirm the pathological characteristics of VASP as well as detection on OPN level. As shown in Fig. 1C, the H&E staining indicated a remarkable thinner plaque fibrous cap and larger lipid core area in the VASP with a high number of cholesterol crystals and inflammatory cell infiltration. Lower collagen content was also observed in the Masson staining of the plaque staining, which affirms pathological characteristics of vulnerable plaques. Expression of CD68 was significantly elevated in AS plaques compared with control vessel tissue suggesting the presence of activated macrophages in abundance within the plaques. Immunohistochemistry staining also displayed a distinct region of OPN expression that well overlapped with the staining region of CD68. This finding implies that the increased OPN level might originate from the activated macrophages. Furthermore, oil red staining was performed on the whole arteries isolated from the bilateral carotid artery to the iliac artery. In comparison with healthy control mice, the carotid arteries of VASP mice exhibited oil red staining on the side where the constriction ring was placed (Fig. 1D). This finding indicates the presence of a large number of fatty plaques on this side of the carotid artery, while the plaques on the contralateral carotid artery have not been formed yet. This might be attributed to the changes in the shear stress of the blood flow caused by the

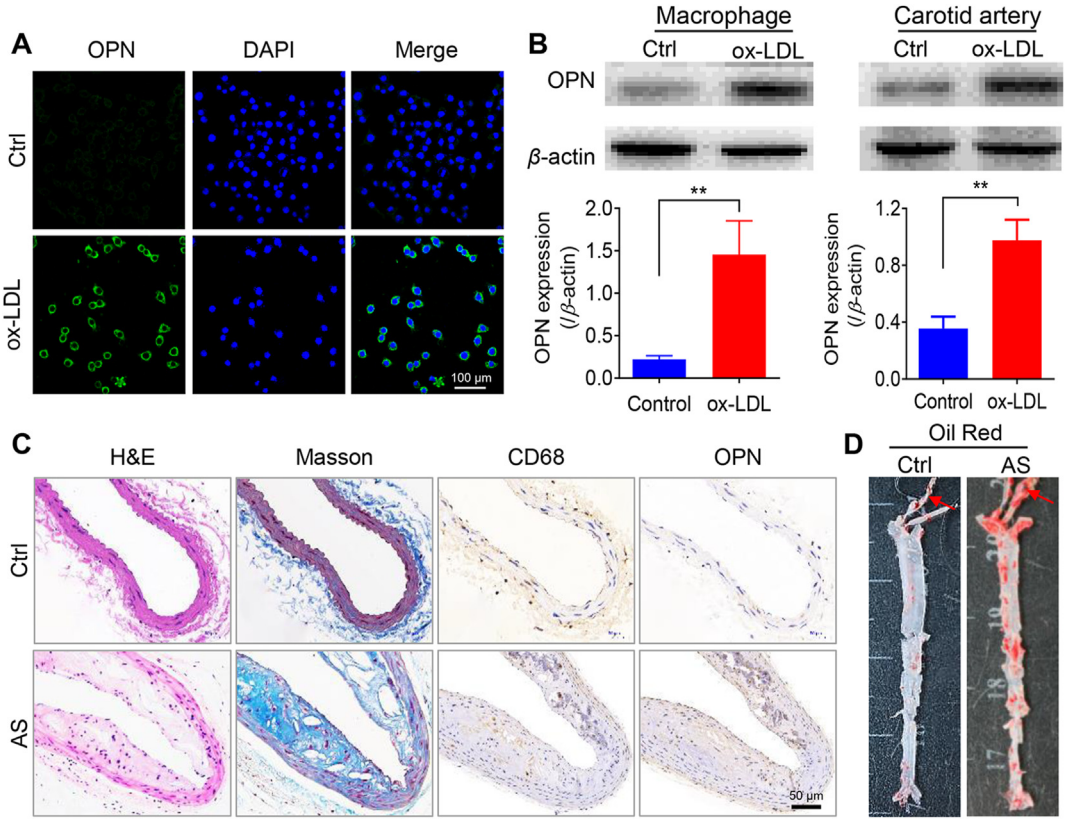

Figure 1 Evaluations of OPN expression in foamy macrophages and vulnerable atherosclerotic plaques. (A) Immunofluorescence images of non-stimulated and stimulated by ox-LDL RAW 264.7 cells ($n = 4$). (B) OPN expression levels in non-stimulated *vs.* stimulated by ox-LDL RAW 264.7 cells and healthy vessels *vs.* vulnerable atherosclerotic plaques evaluated by Western blot analysis. Data are presented as mean ± SD ($n = 5$), $^{**}P < 0.01$. (C) H&E, Masson, and immunohistochemistry staining of CD68 and OPN of segments from carotid arteries isolated from AS mice ($n = 6$). (D) Oil red staining of the whole vessel from bilateral carotid artery to iliac artery obtained from healthy and AS mice. Red arrow indicates atherosclerotic lesion ($n = 4$).

constriction ring, which ultimately leads to easier formulation of vulnerable plaques at the proximal end[11,27,39]. In conclusion, *in vitro* and *ex vivo* findings in this study have verified the successful establishment of VASP in mice and demonstrated increased OPN expression by the stimulated macrophages within atherosclerotic lesions. This overexpression can, therefore, serve as a useful characteristic for targeting moieties of VASPs.

3.2. *Structure and characteristics of NPs*

Given the identification of OPN as targeting moieties of VASPs, NPs were constructed for precise theranostic targeting of VASPs. The theranostic TPZ/IR780@HSA−OPN NPs were formulated from HSA decorated with an OPN-targeting peptide and encapsulated payloads of the hydrophobic NIR photosensitizer IR780 and a hypoxia-activated chemo-drug TPZ. It is believed that the self-assembly of NPs was driven by the hydrophobic interactions between HSA and hydrophobic drug molecules[40]. The control TPZ/IR780@HSA NPs without targeting ability were also constructed from native HSA without antiOPN peptide modification. The TEM images revealed a uniform spherical-shaped morphology of the TPZ/IR780@HSA−OPN and TPZ/IR780@HSA NPs with an average particle size of approximately 170 nm (Fig. 2A). The hydrodynamic diameters (HDs) of the as-prepared NPs were recorded by dynamic light scattering (DLS), which revealed an average size of 190.7 ± 12.5 nm for the TPZ/IR780@HSA NPs and 196.2 ± 7.6 nm for the TPZ/IR780@HSA−OPN NPs. The polydispersity index (PDI) of TPZ/IR780@HSA NPs and TPZ/IR780@HSA−OPN NPs was 0.141 ± 0.013 and 0.176 ± 0.021, respectively (Fig. 2B). This indicated the uniform size distribution of the obtained NPs. The characteristic peaks in the ultraviolet−visible (UV−Vis) absorbance spectra validated the presence of IR780 and TPZ in the TPZ/IR780@HSA−OPN NPs (Fig. 2C). The loading capacity of IR780 and TPZ in the NPs was calculated from the UV−Vis spectra and was determined to be 2.1% and 2.6%, respectively. In addition, we also investigated the *in vitro* TPZ release profile of TPZ/IR780@HSA−OPN NPs in PBS at neutral (pH 7.4) and acidic (pH 6.5) condition. As shown in Supporting Information Fig. S1, TPZ was released from the NPs at a higher rate in acidic conditions than in neutral conditions with no obvious burst effect.

The photodynamic property of the TPZ/IR780@HSA−OPN NPs was assessed by detecting the generation of ROS under NIR laser irradiation (808 nm, 1.0 W/cm^2). The ROS detection was monitored using 1,3-diphenylisobenzofuran (DPBF) as a molecule probe. The absorbance intensity of DPBF at 420 nm irreversibly decreases in the presence of singlet oxygen[20,41]. Fig. 2D indicates that the characteristic absorbance of DPBF attenuated continuously as the laser irradiation was extended, which suggests the generation of ROS by the photosensitizer IR780 encapsulated in the NPs. As shown in Fig. 2E, the TPZ/IR780@HSA−OPN NPs

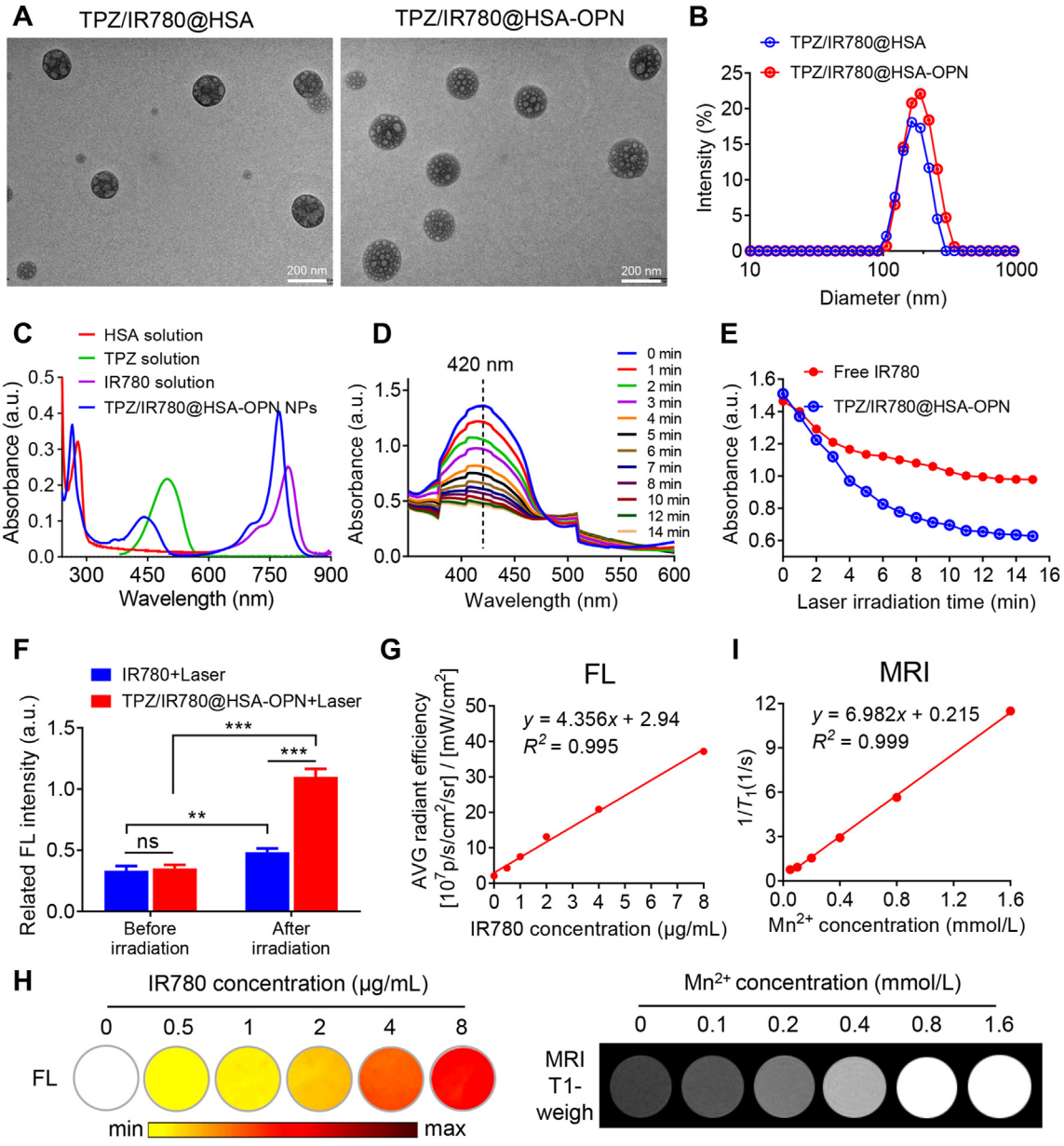

Figure 2 Characterizations of TPZ/IR780@HSA−OPN NPs. (A) Representative TEM image of TPZ/IR780@HSA and TPZ/IR780@HSA−OPN NPs. (B) The hydrodynamic size distribution of TPZ/IR780@HSA and TPZ/IR780@HSA−OPN NPs measured by DLS. The PDI of TPZ/IR780@HSA and TPZ/IR780@HSA−OPN NPs was 0.141 and 0.176, respectively. UV−Vis absorbance spectra of TPZ/IR780@HSA−OPN NPs (C) and the ROS detection probe DPBF under laser irradiation (D). (E) Temporal dependence of characteristic absorbance intensity of DPBF in 420 nm under the light irradiation (808 nm, 1.0 W/cm^2). (F) Fluorescence intensity of MitoXpress probe before and after laser exposure in the presence of free IR780 and TPZ/IR780@HSA−OPN NPs. DPBF was used as the $^1O_2$ scavenger. Data are presented as mean ± SD ($n = 5$), $^{**}P < 0.01$, $^{***}P < 0.001$. (G) Optical and T1-weighted MR phantoms of TPZ/IR780@HSA−OPN NPs aqueous solution at various concentrations. (H) Average radiant efficiency obtained by ROI linear regression analysis against IR780 concentration. (I) Chelate-manganese ion relaxation area efficiency of the TPZ/IR780@HSA−OPN−Ce6 (Mn^{2+}) NPs.

resulted in a significantly greater decrease in the absorbance intensity of DPBF compared with the free IR780. This difference indicates that the TPZ/IR780@HSA−OPN NPs had a more sustainable and stronger PD effect than that of free IR780 molecules. Subsequently, the resulting hypoxia after the NIR laser irradiation was further determined *via* detecting the oxygen consumption using a MitoXpress probe, the fluorescence intensity of which is inversely proportional to the oxygen concentration. The suspension of both the free IR780 and TPZ/IR780@HSA−OPN NPs showed increased fluorescence using MitoXpress, demonstrating consumption of oxygen upon laser irradiation (Fig. 2F). In comparison to the free IR780, the suspension of the TPZ/IR780@HSA−OPN NPs led to a more hypoxic circumvent at the end of the NIR laser irradiation. These findings verify a cascade of effects of the TPZ/IR780@HSA−OPN NPs under laser irradiation, including ROS generation and increased hypoxia level.

To assess the trafficking profile of the NPs *in vivo*, the intrinsic fluorescence property of the TPZ/IR780@HSA−OPN NPs was characterized and the TPZ/IR780@HSA−OPN NPs were conjugated with chlorine e6 (Ce6), which is a chelator for the Mn^{2+} species. The fluorescence intensity of the TPZ/IR780@HSA−OPN NPs showed a linear correlation with the concentration (Fig. 2G). Meanwhile, with increasing concentrations of TPZ/IR780@HSA−OPN NPs, the T1-weighted magnetic resonance imaging (MRI) phantoms were also enhanced (Fig. 2H). The MRI signal increased linearly over a wide range of Mn^{2+} concentrations. The R1 relaxivity that was derived from the slope of the plot of inverse relaxation time (1/T1) *versus* the Mn^{2+} concentration was calculated as 6.92 mmol/L/s (Fig. 2I). Therefore, the *in vivo* biodistribution behavior of TPZ/IR780@HSA−OPN NPs can be readily tracked using both NIR fluorescence imaging and MRI in a non-invasive manner.

3.3. *Targeting ability of TPZ/IR780@HSA−OPN NPs towards foamy macrophages*

Selectivity renders PDT appealing in AS, while other endovascular methods carry a considerable risk of damage to the unaffected cells of the arterial wall. Therefore, the targeting ability of TPZ/IR780@HSA−OPN NPs *in vitro* was investigated by confocal laser scanning microscopy (CLSM) in RAW 264.7 cell lines. Very weak red fluorescence originating from IR780 was detected on the non-activated RAW 264.7 cells after incubation with either non-targeted TPZ/IR780@HSA or targeted TPZ/IR780@HSA−OPN NPs for 24 h (Fig. 3A). However, the foamy macrophages that were polarized upon stimulation of ox-LDL exhibited distinct fluorescence after incubation with the TPZ/IR780@HSA−OPN NPs, while a weak signal was observed in the foamy macrophages incubated with the non-targeted NPs. Interestingly, the mean fluorescence intensity was markedly decreased in the foamy macrophages that were pre-treated with antiOPN peptide for 1 h prior to the addition of the TPZ/IR780@HSA−OPN NPs ($P < 0.001$, Fig. 3B). In addition, we conducted the flow cytometry to quantify the targeting ability of nanoprobes towards RAW 264.7 cells and ox-LDL stimulated foamy macrophages. As presented in Fig. 3C, the IR780 fluorescence intensity of foamy macrophages treated with TPZ/IR780@HSA−OPN NPs group was significantly higher than that of other groups. When pre-treated with antiOPN peptide, the foamy macrophages incubated with the TPZ/IR780@HSA−OPN NPs showed obviously decreased fluorescence intensity, which agrees with the observations by CLSM. The obtained data suggests that the strong binding affinity is mediated by the OPN-targeting peptide localized in the NPs, thus providing an improved recognition of foamy macrophages with further increased cellular penetration and accumulation.

3.4. *VASPs-targeting ability of TPZ/IR780@HSA−OPN NPs in vivo*

The pathological staining confirmed the formation of carotid vulnerable plaques in mice with an AS model. The trafficking behavior of the NPs was continuously monitored by NIR fluorescence imaging *in vivo* for 8 h after intravenous injection of TPZ/IR780@HSA−OPN NPs or TPZ/IR780@HSA NPs (Fig. 4A). A distinct fluorescence signal was observed in which the cast was placed in the left carotid artery of the AS model mice injected with TPZ/IR780@HSA−OPN NPs. However, no obvious fluorescence signal was found in the AS model mice injected with TPZ/IR780@HSA NPs or in the healthy mice injected with TPZ/IR780@HSA−OPN NPs (Fig. 4B and C). The strongest signals appeared at the time point of 30 min after injection, and then gradually attenuated with time elapsing. Arteries were also

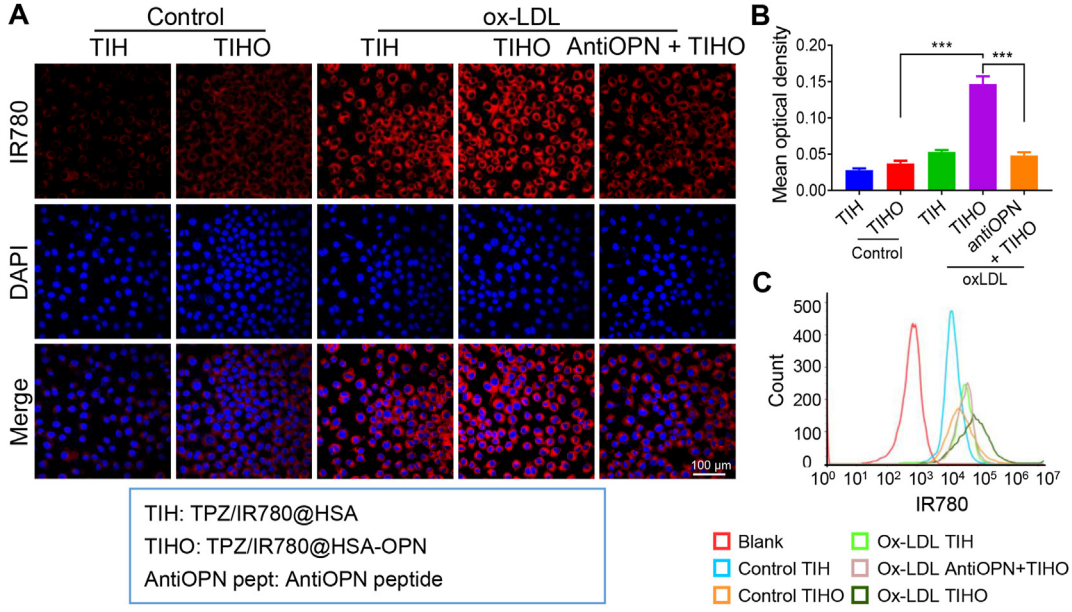

Figure 3 Targeting ability of TPZ/IR780@HSA−OPN NPs toward foamy macrophages. (A) CLSM images of RAW 264.7 cells and stimulated foamy macrophages incubated with TPZ/IR780@HSA NPs or TPZ/IR780@HSA−OPN NPs. (B) Mean optical density of the same treated groups (mean ± SD, $n = 5$, $^{***}P < 0.001$). (C) The IR780 fluorescence intensity of RAW 264.7 cells and stimulated foamy macrophages incubated with TPZ/IR780@HSA NPs or TPZ/IR780@HSA−OPN NPs measured by Flow cytometry of the same treated group. RAW 264.7 cells that were not incubated with the nanoprobes were used as blank control.

isolated for *ex vivo* study 1 h after injection. The *ex vivo* fluorescence imaging revealed that TPZ/IR780@HSA−OPN NPs had a higher ($P < 0.01$) affinity to the carotid plaques in the AS model mice in comparison to the other groups (Fig. 4D and E). To further confirm the accumulation of TPZ/IR780@HSA−OPN NPs in the vulnerable plaques, immunofluorescence staining was conducted after *ex vivo* fluorescence imaging. A strong fluorescence from IR780 was detected in the carotid vulnerable plaques of the AS model mice administered TPZ/IR780@HSA−OPN NPs and co-localized with signals of the macrophage marker CD68 in comparison with the control groups ($P < 0.01$), as shown in Fig. 4F and G. Furthermore, *in vivo* MR imaging was carried out to verify the vulnerable plaque-targeting ability of nanoprobe. A 7.0 T MR imaging platform was used for 8 h after the TPZ/IR780@HSA−OPN NPs and TPZ/IR780@HSA NPs were injected (Fig. 4A). No significant enhanced T1-weighted MR signals were observed in both sides of the carotid artery in the healthy mice injected with TPZ/IR780@HSA−OPN NPs and the AS model mice injected with TPZ/IR780@HSA NPs (Fig. 4H and I). However, the OPN-targeted TPZ/IR780@HSA−OPN NPs was found to remarkably enhance the T1-weighted MR signals of the carotid plaques in the model mice, with peak signals appearing 2 h after the injection. These fluorescence/MR dual-modal imaging results support that the OPN-targeted TPZ/IR780@HSA−OPN NPs could selectively accumulate in the VASP lesions profiling from the OPN-mediated targeting.

3.5. *Therapeutic efficacy of TPZ/IR780@HSA−OPN NPs in vitro*

The ability of TPZ/IR780@HSA−OPN NPs to induce intracellular ROS production and increase hypoxia conditions upon NIR irradiation was investigated *in vitro* through CLSM using a hypoxia/ROS detection probe. Foamy RAW 264.7 cells activated with ox-LDL were incubated with TPZ/IR780@HSA−OPN NPs or free IR780 for 24 h, followed by NIR irradiation for 5 min. As shown in Fig. 5A, B and C, strong green and purple intracellular fluorescence were detected in the cells incubated with TPZ/IR780@HSA−OPN NPs, indicating an elevated amount of ROS generation and hypoxia inside foamy macrophages upon laser irradiation ($P < 0.001$). On the contrary, negligible fluorescence was detected in the cells that were treated with free IR780, suggesting considerably diminished ROS amount and hypoxia levels due to low cellular uptake of free dye. The cells treated with ROS inducer (pyocyanin, Pyo) or hypoxia inducer (deferoxamine, DFO) were employed as the positive controls ($P < 0.001$). These experimental observations revealed a high level of ROS and laser-enhanced hypoxia in the cells treated with TPZ/IR780@HSA−OPN NPs, which was expected to trigger the biotoxicity of TPZ. The synergistic therapy efficacy originating from the laser irradiation induced a cascade of events that were also quantitatively determined by a Cell Counting Kit-8 (CCK-8) assay and flow cytometry assay. As presented in Fig. 5D, the viability of macrophages was dependent on the concentration of the used NPs for all the cell groups. Incubation of macrophages with TPZ/IR780@HSA−OPN NPs without laser exposure at concentrations lower than 64 μg/mL, did not cause a significant decrease in the cell viability, suggesting a negligible toxicity of TPZ under normoxia. In contrast, cells treatment with IR780@HSA−OPN NPs followed by laser irradiation resulted in significant reduction of cell viability—even at the lowest tested concentration of NPs (4 μg/mL)—which was attributed to the intracellular generations of ROS by IR780@HSA−OPN NPs. Notably, macrophages treated with TPZ/IR780@HSA−OPN NPs and laser irradiated, showed the lowest viabilities at all the tested concentrations with respect to the other cell groups. This result clearly indicated the synergistic therapy efficacy due to laser-induced cascade of ROS generation and TPZ activation. In addition, the apoptosis profiles of the foamy macrophages with various treatments were assessed *via* the Annexin V-FITC/PI apoptosis detection assay. As shown in Fig. 5E, laser irradiation or treatment with TPZ/IR780@HSA−OPN NPs alone caused a very mild cell apoptosis. However, treatment with IR780@HSA−OPN NPs, followed by laser irradiation led to $62.23 \pm 6.42\%$ of apoptotic cells. We also observed that treatment with TPZ/IR780@HSA−OPN NPs, followed by laser irradiation resulted in the highest ratio of apoptotic cells ($79.78 \pm 6.48\%$). Collectively, these results confirmed that the consumption of oxygen by TPZ/IR780@HSA−OPN NPs upon laser irradiation was able to create sufficient hypoxia to activate the encapsulated TPZ and efficient cell killing driven by the synergy between IR780 and TPZ was successfully achieved in response to laser irradiation.

3.6. *Therapeutic efficacy of TPZ/IR780@HSA−OPN NPs in vivo*

The *in vivo* anti-AS outcomes after PDT were assessed in the $ApoE^{-/-}$ mice with VASPs using MR imaging. Similar to the previous *in vitro* experiments, the mice were divided into four groups, including TPZ/IR780@HSA−OPN NPs (−), IR780@HSA−OPN NPs (+), TPZ/IR780@HSA NPs (+), and TPZ/IR780@HSA−OPN NPs (+). As depicted in Fig. 6A, the left carotid area was irradiated with an 808 nm laser at 0.75 W/cm^2 for 3 min following the injection of therapeutic nanoformulations, and the mice underwent MR imaging at the end of treatment for therapeutic evaluations. As shown in Fig. 6B, the 3D reconstitution of time of flight angiography (TOF) indicated that the carotid artery stenosis of mice treated with TPZ/IR780@HSA−OPN NPs (−) displayed no notable throughout the treatment. In contrast, the treatment with TPZ/IR780@HSA−OPN NPs (+) realized obvious recovery of blood perfusion and significant amelioration on the carotid artery stenosis. The differences are suggestive of the potent PDT efficacy and the activation of TPZ upon laser irradiation. The T1-weighted MR signal arising from the lipid contents in the plaque was also employed to characterize the therapy efficacy. As showed in Fig. 6C and D, the quantification of the T1-weighted MR signal showed a remarkable downward trend after treatment with TPZ/IR780@HSA−OPN NPs (+). The impressive efficacy of TPZ/IR780@HSA−OPN NPs (+) was attributed to the substantial apoptosis of foamy macrophages by generated ROS and activated TPZ under laser exposure. Particularly, compared to the TPZ/IR780@HSA−OPN NPs (+), treatment with TPZ/IR780@HSA NPs (+) only induced mild decrease of plaque area and blood perfusion recovery, which should be ascribed to the compromised targeting ability to plaque in the absence of OPN peptide. Following the treatment, carotid arteries segments were also collected for further pathological examinations, including H&E, Masson, and immunohistochemistry staining. The results revealed significant decrease of the foamy macrophages abundance and expansion of collagen region in vulnerable plaques in the AS mice treated with

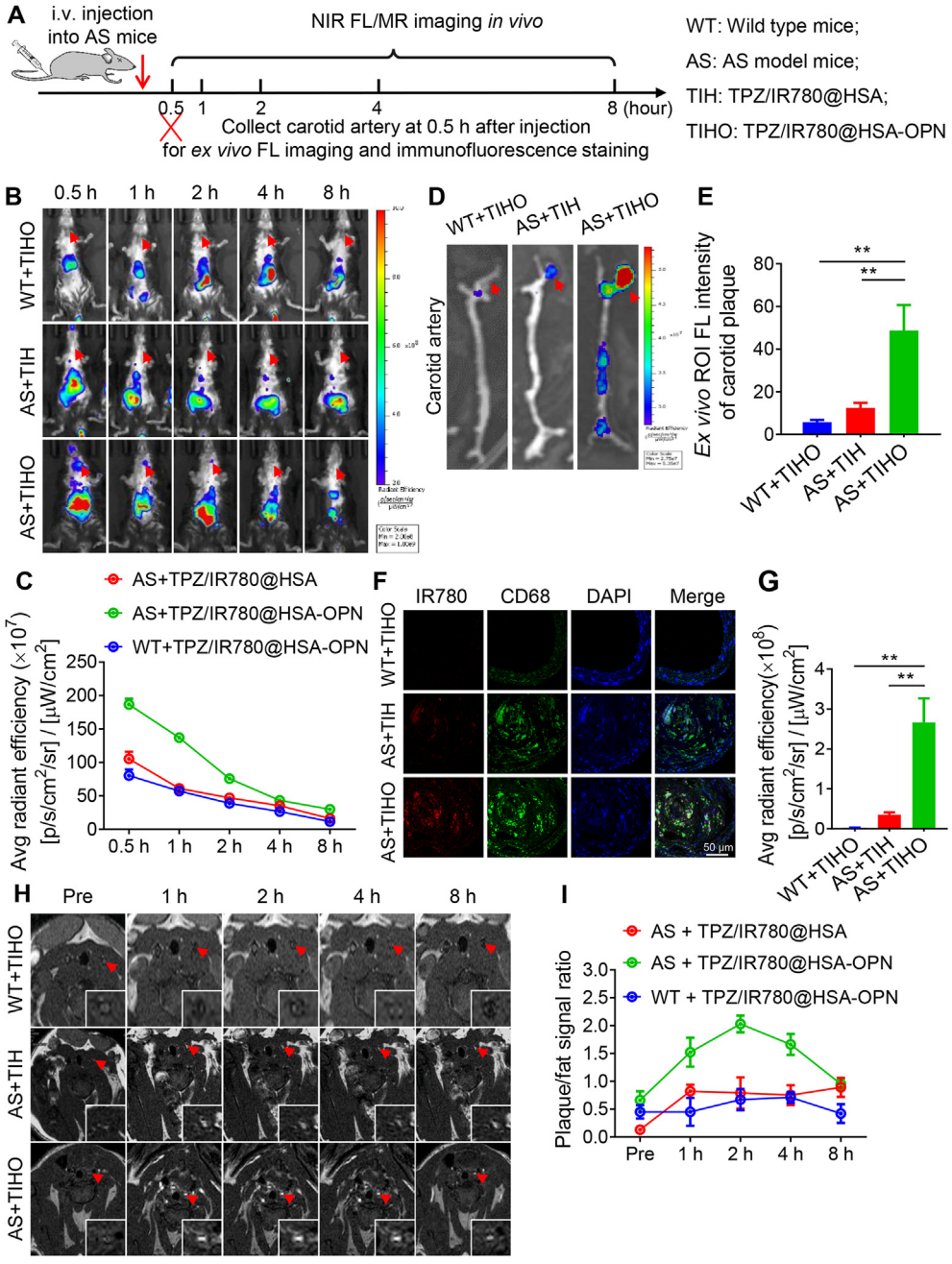

Figure 4 Vulnerable plaques-targeting ability of TPZ/IR780@HSA−OPN NPs *in vivo* and *ex vivo*. (A) Experimental outline of the animal imaging. (B) *In vivo* fluorescence imaging of healthy control mice and AS mice after 0.5, 1, 2, 4 and 8 h of administration with TPZ/IR780@HSA NPs or TPZ/IR780@HSA−OPN NPs. Red arrow indicates atherosclerotic lesion. *Ex vivo* fluorescence images (C) and fluorescence signal quantitative analysis (D) of isolated arteries from healthy mice treated with TPZ/IR780@HSA−OPN NPs, AS mice treated with TPZ/IR780@HSA NPs, and AS mice treated with TPZ/IR780@−OPN NPs (mean ± SD, $n = 10$, $^{**}P < 0.01$). Red arrow indicates atherosclerotic lesion. (E) Average radiant efficiency from healthy control mice and AS mice after 0.5, 1, 2, 4 and 8 h administration with TPZ/IR780@HSA NPs or TPZ/IR780@HSA−OPN NPs. (F) T1-weighted MR images of carotid arteries of healthy control mice and AS mice before and after 1, 2, 4 and 8 h administration with TPZ/IR780@HSA NPs or TPZ/IR780@HSA−OPN NPs. (G) Quantitative analysis of T1-weighted MRI signal changes in carotid artery of ApoE$^{-/-}$ mice before and after 1, 2, 4 and 8 h of administration with TPZ/IR780@HSA NPs or TPZ/IR780@HSA−OPN NPs. (We calculated signal intensity of carotid plaque to fat ratio, the signal intensity of carotid plaque divided by the signal intensity of the subcutaneous fat near the plaque, $n = 10$). (H) The co-localization of the macrophage marker CD68 and IR780 by CLSM in carotid plaques from healthy control mice and AS mice injected with TPZ/IR780@HSA NPs or TPZ/IR780@HSA−OPN NPs. (I) Average radiant efficiency from isolated carotid arteries from healthy mice treated with TPZ/IR780@HSA−OPN NPs, AS mice treated with TPZ/IR780@HSA NPs, and AS mice treated with TPZ/IR780@HSA−OPN NPs (mean ± SD, $n = 10$, $^{**}P < 0.01$).

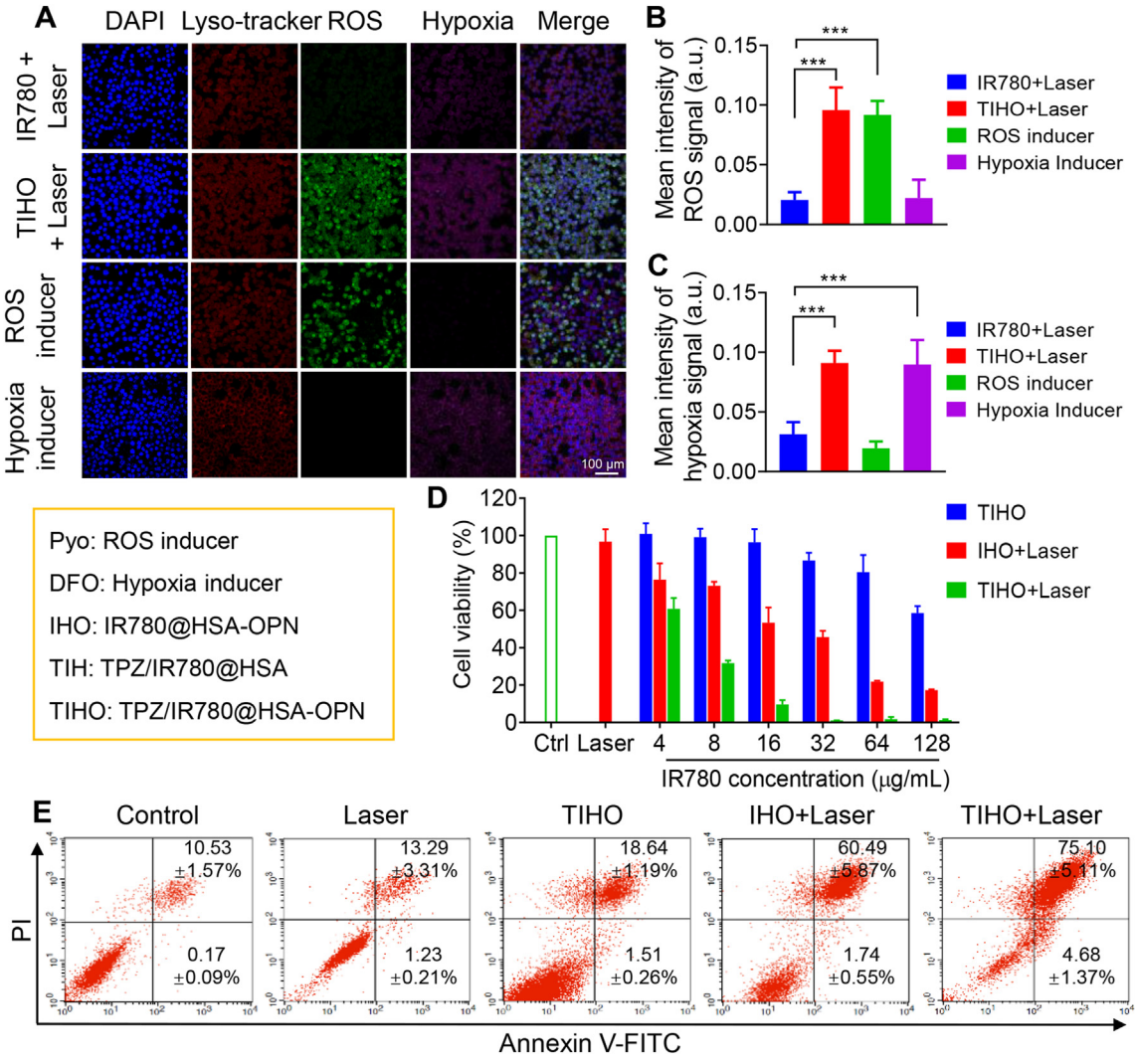

Figure 5 *In vitro* therapeutic efficacy of TPZ/IR780@HSA−OPN NPs-mediated therapy. (A) Representative fluorescence images of foamy macrophages after 24 h incubation with free IR780 or TPZ/IR780@HSA−OPN NPs under 808 nm laser irradiation. Foamy macrophages treated with Pyo or DFO inducers were used as positive controls. Mean intensity of the fluorescence signals arising from ROS (B) and Hypoxia (C) channels in Fig. 5A. Data are presented as mean ± SD ($n = 5$), ***$P < 0.001$. (D) Cell viability of foamy macrophages incubated with TPZ/IR780@HSA−OPN NPs (−), IR780@HSA−OPN (+), and TPZ/IR780@HSA−OPN NPs (+) at different concentrations of IR780 for 24 h (mean ± SD, $n = 5$). (E) Apoptosis ratios of foamy macrophages incubated with TPZ/IR780@HSA−OPN NPs (+), IR780@HSA−OPN NPs (+), and TPZ/IR780@HSA−OPN NPs (+) for 24 h by flow cytometry analysis (mean ± SD, $n = 5$).

IR780@HSA−OPN(+) and TPZ/IR780@HSA−OPN NPs (+) (Fig. 6 E, F, G and H), suggestive of improved plaque stability. Meanwhile, the collagen volume fraction and average optical density of CD68 and OPN showed no significant difference between the treatments of TPZ/IR780@HSA−OPN NPs (−) and TPZ/IR780@HSA NPs (+) groups. Taken together, illustrating that only OPN-targeted nanoprobes under 808 nm laser irradiation could perform the photodynamic effect efficiently.

3.7. Biocompatibility of TPZ/IR780@HSA−OPN NPs

The biocompatibility of nanoprobes also has a significant impact on achieving clinical value. To assess the potential *in vivo* toxicity of the TPZ/IR780@HSA−OPN NPs, hemolytic activity assay was performed by incubating mouse blood red cells with TPZ/IR780@HSA−OPN NPs at various concentrations. The hemolytic assay indicated that the TPZ/IR780@HSA−OPN NPs had no distinct hemolytic activity in comparison with the Triton X-100 positive control group (Supporting Information Fig. S2). Even when incubated with NPs at a fairly high concentration of 128 μg/mL (IR780), the hemolysis ratio of the blood sample was less than 3.4%. This ratio is much lower than that of the internationally recognized standard, according to the degree of hemolysis (< 2.0% non-hemolytic; 2.0%−5.0% slightly hemolytic; and > 5.0% hemolytic) from the ASTM D756 (American Society for Testing and Materials Designation) classification[42]. These outcomes indicate that the TPZ/IR780@HSA−OPN NPs possessed prominent hemocompatibility in the tested

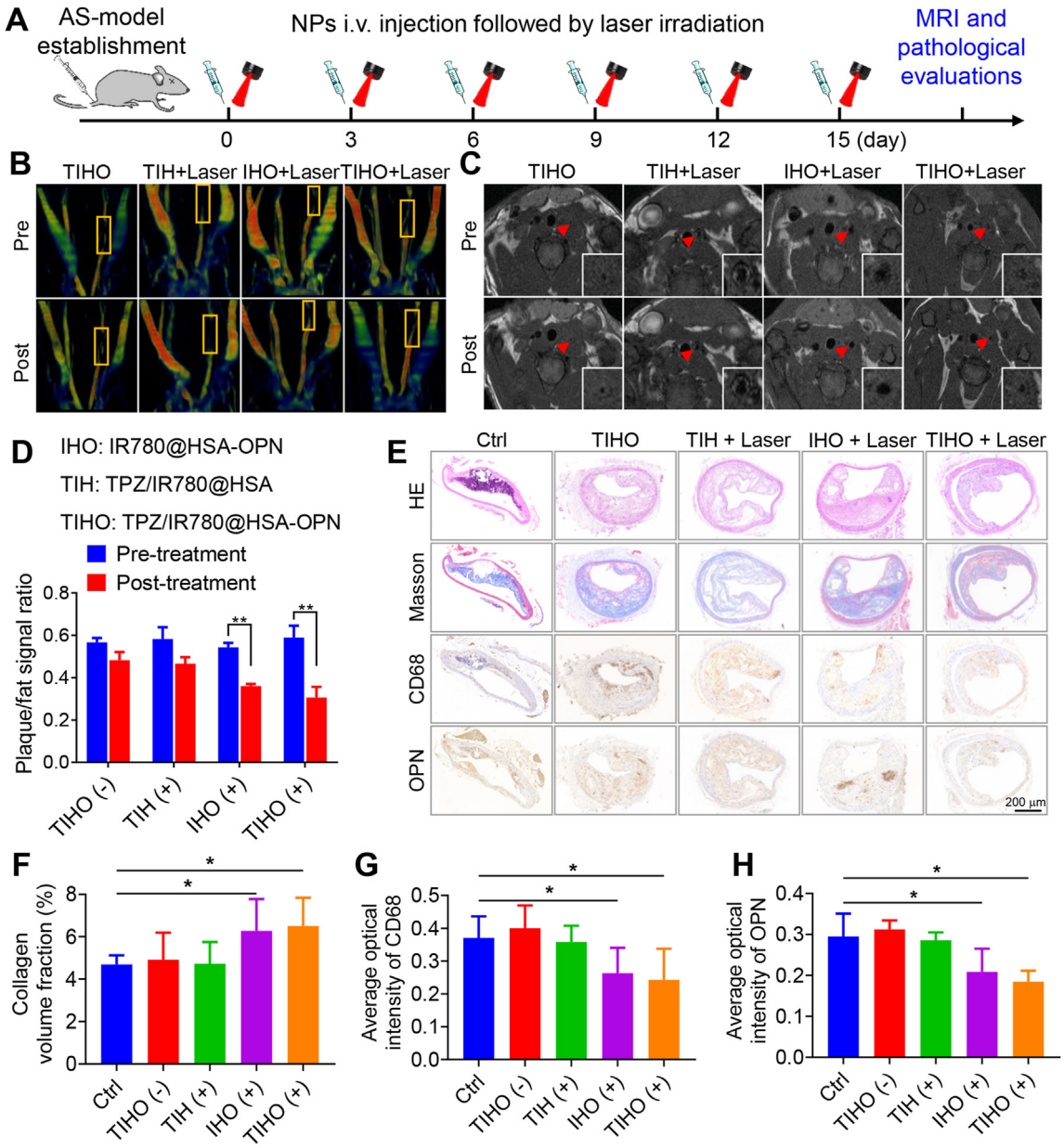

Figure 6 *In vivo* therapeutic efficacy of TPZ/IR780@HSA−OPN NPs-mediated therapy. (A) Experimental illustrations on the animal therapy. T1-weighted MR images (B) and TOF angiography (C) before and after 15 days of treatment with TPZ/IR780@HSA−OPN NPs (−), TPZ/IR780@HSA NPs (+), IR780@HSA−OPN NPs (+), and TPZ/IR780@HSA−OPN NPs (+). (D) Quantitative analysis on the Plaque/Fat signal ratio derived from Fig. 6C (mean ± SD, $n = 10$, $^{**}P < 0.01$). (E) Histological analysis with H&E, Masson and immunohistochemistry staining of the carotid artery segments isolated from AS mice of different treatment groups. Collagen volume fraction (F), average optical intensity of CD68 (G), and average optical intensity of OPN (H) of carotid artery extracted from different treatment groups (mean ± SD, $n = 10$), $^{*}P < 0.05$. (+) represents 808 nm laser irradiation; (−) no laser irradiation.

concentration range. Mouse blood was also collected for blood bio chemistry analysis at 1 and 24 h after the treatment with TPZ/IR780@HSA−OPN NPs (+). As showed in Fig. 7A, the administration of TPZ/IR780@HSA−OPN NPs did not cause significant alteration ($P > 0.05$) on the levels of biochemical blood biomarkers (ALT, AST, GGT, TBIL, Cr, GLU, BUN, CK-MB, LDH, GSP, CK, and UA) compared to control injected with PBS (pH 7.4). This finding demonstrates no obvious damage to liver, renal, and cardiac function and little risk of diabetes mellitus after treatment with TPZ/IR780@HSA−OPN NPs. In order to evaluate the toxicity of the NPs at the histological level, the major organs of the mice at the end of treatment with TPZ/IR780@HSA−OPN NPs (1 mg/kg) or TPZ/IR780@HSA−OPN NPs (1 mg/kg) combined with laser irradiation were harvested for H&E staining. Compared to the untreated healthy mice, neither of the treatments resulted in any overt tissue damage (Fig. 7B). These results provide compelling evidence for the favorable biocompatibility of TPZ/IR780@HSA−OPN NPs.

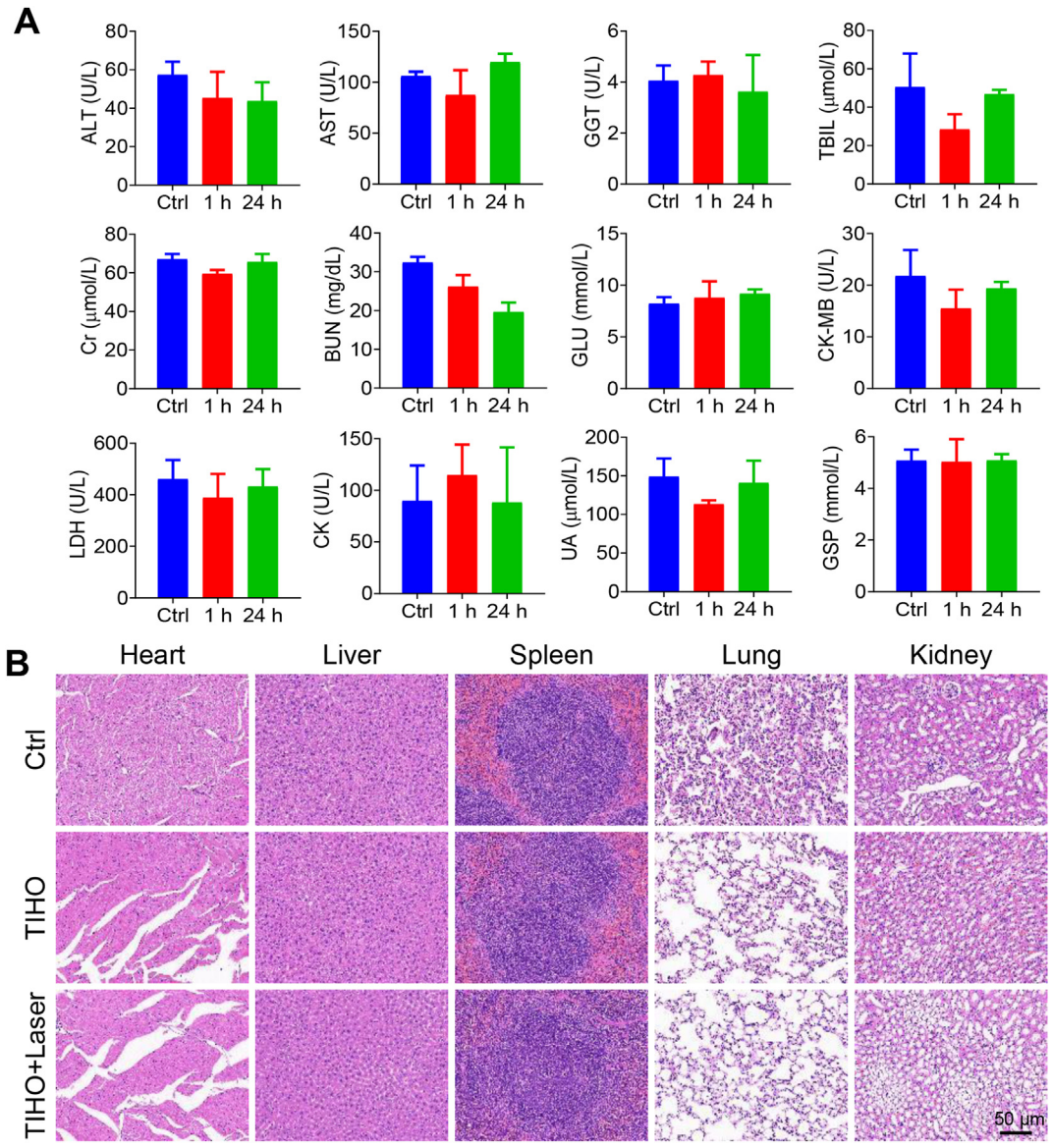

Figure 7 Biosafety evaluations on the treatment with TPZ/IR780@HSA−OPN NPs. (A) Mice blood was collected 1 and 24 h after TPZ/IR780@HSA−OPN NPs-mediated PDT was finished and untreated mice blood was used as control group. The blood samples from each group was used to test liver function indexes (ALT, AST, TBIL, and GGT), renal function indexes (Cr, BUN, and UA), cardiac function indexes (CK, CK-MB, and LDH-L), and glucose levels (GLU, GSP) (mean ± SD, $n = 5$). (B) H&E-stained images of major organs (heart, liver, spleen, lungs, and kidneys) extracted from untreated mice, treated with TPZ/IR780@HSA−OPN NPs (−) or TPZ/IR780@HSA−OPN NPs (+). (+) represents 808 nm laser irradiation; (−) no laser exposure.

4. Conclusions

In conclusion, we have fabricated high biocompatible HSA-based OPN-targeted NPs, which demonstrated a great potential for AS treatment. Elevated expression of OPN in foamy macrophages and atherosclerotic lesions served as a target for precise identification and therapy of VASPs. High specificity of OPN-targeted NPs was observed by dual fluorescence and MR imaging *in vivo* and *ex vivo*. Furthermore, NPs-mediated PDT selectively induced apoptosis of foamy macrophages in non-invasive manner by releasing ROS under 808 nm laser irradiation, thereby, inhibiting plaque progression, improving plaque stability, and alleviating the progress of the vascular stenosis. In comparison to the existing clinical therapeutic methods, NPs-mediated PDT has number of advantages including specifically targeting the vulnerable plaques and low damage to normal tissues and cells adjacent to the plaques. Experimental outcomes of our study provide novel insights into the development of PDT-based multifunctional stimuli-responsive platforms for efficient AS treatment.

Acknowledgments

This work was supported by the National Nature Science Foundation of China (Nos. 81820108019, 91939303 and 31971302), the National Key Research and Development Program of China (2018YFC0116305), and the Science Foundation of PLA General Hospital (2018XXFC-9, CX19028, China).

Author contributions

Mengqi Xu and Cong Mao designed and performed the experiments and analyzed the data. Haoting Chen, Lu Liu, Yabin Wang and Sulei Li helped perform the experiments. Mengqi Xu, Ruslan G. Tuguntaev and Abid Hussain wrote the manuscript. Xu Zhang, Xing-Jie Liang, Weisheng Guo and Feng Cao contributed to conception of the work and manuscript revision. Feng Cao and Weisheng Guo was responsible for supervision. All of the authors have read and approved the final manuscript.

Conflicts of interest

The authors declare that they have no conflict of interest.

Appendix A. Supporting information

Supporting data to this article can be found online at https://doi.org/10.1016/j.apsb.2021.12.020.

References

1. Benjamin EJ, Blaha MJ, Chiuve SE, Cushman M, Das SR, Deo R, et al. Heart disease and stroke statistics—2017 update: a report from the american heart association. *Circulation* 2017;**135**:e146–603.
2. Collura S, Morsiani C, Vacirca A, Fronterrè S, Ciavarella C, Vasuri F, et al. The carotid plaque as paradigmatic case of site-specific acceleration of aging process: the micrornas and the inflammaging contribution. *Ageing Res Rev* 2020;**61**:101090.
3. Libby P, Buring JE, Badimon L, Hansson GK, Deanfield J, Bittencourt MS, et al. Atherosclerosis. *Nat Rev Dis Primers* 2019;**5**:56.
4. Yan J, Horng T. Lipid metabolism in regulation of macrophage functions. *Trends Cell Biol* 2020;**30**:979–89.
5. Sakakura K, Nakano M, Otsuka F, Ladich E, Kolodgie FD, Virmani R. Pathophysiology of atherosclerosis plaque progression. *Heart Lung Circ* 2013;**22**:399–411.
6. Dahl TB, Yndestad A, Skjelland M, Øie E, Dahl A, Michelsen A, et al. Increased expression of visfatin in macrophages of human unstable carotid and coronary atherosclerosis: possible role in inflammation and plaque destabilization. *Circulation* 2007;**115**:972–80.
7. Saidoune F, Even G, Lamri Y, Chezel J, Gaston AT, Escoubet B, et al. Effects of baff neutralization on atherosclerosis associated with systemic lupus erythematosus. *Arthritis Rheumatol* 2021;**73**:255–64.
8. Hadamitzky M. Machine learning for ischemia prediction CTA: perspective toward the noninvasive one-stop shop for stable cad? *JACC Cardiovasc Imaging* 2021;**14**:642–3.
9. Bytyçi I, Shenouda R, Wester P, Henein MY. Carotid atherosclerosis in predicting coronary artery disease: a systematic review and meta-analysis. *Arterioscler Thromb Vasc Biol* 2021;**41**:e224–37.
10. Arbab-Zadeh A, Fuster V. From detecting the vulnerable plaque to managing the vulnerable patient: *JACC* state-of-the-art review. *J Am Coll Cardiol* 2019;**74**:1582–93.
11. Bourantas CV, Räber L, Sakellarios A, Ueki Y, Zanchin T, Koskinas KC, et al. Utility of multimodality intravascular imaging and the local hemodynamic forces to predict atherosclerotic disease progression. *JACC Cardiovasc Imaging* 2020;**13**:1021–32.
12. Kyaw T, Peter K, Li Y, Tipping P, Toh BH, Bobik A. Cytotoxic lymphocytes and atherosclerosis: significance, mechanisms and therapeutic challenges. *Br J Pharmacol* 2017;**174**:3956–72.
13. Bom MJ, van der Heijden DJ, Kedhi E, van der Heyden J, Meuwissen M, Knaapen P, et al. Early detection and treatment of the vulnerable coronary plaque: can we prevent acute coronary syndromes?. *Circ Cardiovasc Imaging* 2017;**10**:e005973.
14. Chen J, Zhang X, Millican R, Sherwood J, Martin S, Jo H, et al. Recent advances in nanomaterials for therapy and diagnosis for atherosclerosis. *Adv Drug Deliv Rev* 2021;**170**:142–99.
15. Abdelrahman KM, Chen MY, Dey AK, Virmani R, Finn AV, Khamis RY, et al. Coronary computed tomography angiography from clinical uses to emerging technologies: JACC state-of-the-art review. *J Am Coll Cardiol* 2020;**76**:1226–43.
16. Head SJ, Milojevic M, Daemen J, Ahn JM, Boersma E, Christiansen EH, et al. Mortality after coronary artery bypass grafting *versus* percutaneous coronary intervention with stenting for coronary artery disease: a pooled analysis of individual patient data. *Lancet* 2018;**391**:939–48.
17. Doenst T, Haverich A, Serruys P, Bonow RO, Kappetein P, Falk V, et al. PCI and CABG for treating stable coronary artery disease: JACC review topic of the week. *J Am Coll Cardiol* 2019;**73**:964–76.
18. Gallone G, Baldetti L, Pagnesi M, Latib A, Colombo A, Libby P, et al. Medical therapy for long-term prevention of atherothrombosis following an acute coronary syndrome: JACC state-of-the-art review. *J Am Coll Cardiol* 2018;**72**:2886–903.
19. Chan CKW, Zhang L, Cheng CK, Yang H, Huang Y, Tian XY, et al. Recent advances in managing atherosclerosis *via* nanomedicine. *Small* 2018;**14**:1702793.
20. Liu Y, Zhen W, Jin L, Zhang S, Sun G, Zhang T, et al. All-in-one theranostic nanoagent with enhanced reactive oxygen species generation and modulating tumor microenvironment ability for effective tumor eradication. *ACS Nano* 2018;**12**:4886–93.
21. Kwon S, Ko H, You DG, Kataoka K, Park JH. Nanomedicines for reactive oxygen species mediated approach: an emerging paradigm for cancer treatment. *Acc Chem Res* 2019;**52**:1771–82.
22. Mitchell MJ, Billingsley MM, Haley RM, Wechsler ME, Peppas NA, Langer R. Engineering precision nanoparticles for drug delivery. *Nat Rev Drug Discov* 2020;**20**:104–24.
23. Zhang MJ, Zhou Y, Chen L, Wang YQ, Wang X, Pi Y, et al. An overview of potential molecular mechanisms involved in VSMC phenotypic modulation. *Histochem Cell Biol* 2016;**145**:119–30.
24. Tanaka F, Ozawa Y, Inage Y, Deguchi K, Itoh M, Imai Y, et al. Association of osteopontin with ischemic axonal death in periventricular leukomalacia. *Acta Neuropathol* 2000;**100**:69–74.
25. Borrell-Pagès M, Romero JC, Juan-Babot O, Badimon L. Wnt pathway activation, cell migration, and lipid uptake is regulated by low-density lipoprotein receptor-related protein 5 in human macrophages. *Eur Heart J* 2011;**32**:2841–50.
26. Qiao H, Wang Y, Zhang R, Gao Q, Liang X, Gao L, et al. MRI/optical dual-modality imaging of vulnerable atherosclerotic plaque with an osteopontin-targeted probe based on Fe_3O_4 nanoparticles. *Biomaterials* 2017;**112**:336–45.
27. Qiao R, Qiao H, Zhang Y, Wang Y, Chi C, Tian J, et al. Molecular imaging of vulnerable atherosclerotic plaques *in vivo* with osteopontin-specific upconversion nanoprobes. *ACS Nano* 2017;**11**:1816–25.
28. Zhang J, Zu Y, Dhanasekara CS, Li J, Wu D, Fan Z, et al. Detection and treatment of atherosclerosis using nanoparticles. *Wiley Interdiscip Rev Nanomed Nanobiotechnol* 2017;**9**:e1412.
29. Li X, Lovell JF, Yoon J, Chen X. Clinical development and potential of photothermal and photodynamic therapies for cancer. *Nat Rev Clin Oncol* 2020;**17**:657–74.
30. Rockson SG, Lorenz DP, Cheong WF, Woodburn KW. Photoangioplasty: an emerging clinical cardiovascular role for photodynamic therapy. *Circulation* 2000;**102**:591–6.
31. Jain M, Zellweger M, Wagnieres G, van den Bergh H, Cook S, Giraud MN. Photodynamic therapy for the treatment of atherosclerotic plaque: lost in translation? *Cardiovasc Ther* 2017;**35**:e12238.
32. Zhen X, Cheng P, Pu K. Recent advances in cell membrane-camouflaged nanoparticles for cancer phototherapy. *Small* 2019;**15**:e1804105.
33. Deng X, Shao Z, Zhao Y. Solutions to the drawbacks of photothermal and photodynamic cancer therapy. *Adv Sci* 2021;**8**:2002504.

34. Lin F, Bao YW, Wu FG. Improving the phototherapeutic efficiencies of molecular and nanoscale materials by targeting mitochondria. *Molecules* 2018;**23**:3016.
35. Liu T, Ma X, Ouyang T, Chen H, Xiao Y, Huang Y, et al. Efficacy of 5-aminolevulinic acid-based photodynamic therapy against keloid compromised by downregulation of SIRT1-SIRT3-SOD2-mROS dependent autophagy pathway. *Redox Biol* 2019;**20**: 195−203.
36. Cheng C, Tempel D, van Haperen R, van der Baan A, Grosveld F, Daemen MJ, et al. Atherosclerotic lesion size and vulnerability are determined by patterns of fluid shear stress. *Circulation* 2006;**113**: 2744−53.
37. Ma S, Motevalli SM, Chen J, Xu MQ, Wang Y, Feng J, et al. Precise theranostic nanomedicines for inhibiting vulnerable atherosclerotic plaque rrogression through regulation of vascular smooth muscle cell phenotype switching. *Theranostics* 2018;**8**:3693−706.
38. Ding Y, Zhang M, Zhang W, Lu Q, Cai Z, Song P, et al. Amp-activated protein kinase alpha 2 deletion induces vsmc phenotypic switching and reduces features of atherosclerotic plaque stability. *Circ Res* 2016; **119**:718−30.
39. Ford TJ, Berry C, De Bruyne B, Yong ASC, Barlis P, Fearon WF, et al. Physiological predictors of acute coronary syndromes: emerging insights from the plaque to the vulnerable patient. *JACC Cardiovasc Interv* 2017;**10**:2539−47.
40. Liu L, Hu F, Wang H, Wu X, Eltahan AS, Stanford S, et al. Secreted protein acidic and rich in cysteine mediated biomimetic delivery of methotrexate by albumin-based nanomedicines for rheumatoid arthritis therapy. *ACS Nano* 2019;**13**:5036−48.
41. Vankayala R, Lin CC, Kalluru P, Chiang CS, Hwang KC. Gold nanoshells-mediated bimodal photodynamic and photothermal cancer treatment using ultra-low doses of near infra-red light. *Biomaterials* 2014;**35**:5527−38.
42. Barbosa AA, Júnior SA, Mendes RL, de Lima RS, de Vasconcelos Ferraz A. Multifunctional hydroxyapatite with potential for application in theranostic nanomedicine. *Mater Sci Eng C Mater Biol Appl* 2020;**116**:111227.